Journal of Electronic Imaging 11(1), 1–0 (January 2002).

Comparison of deconvolution techniques using a distribution mixture parameter estimation: Application in single photon emission computed tomography imagery

M. Mignotte
DIRO, Département d'Informatique et de Recherche Opérationnelle
C.P. 6128
Succ. Centre-ville
Montréal (Québec) H3C 3J7 Canada
E-mail: mignotte@iro.umontreal.ca

J. Meunier
INRIA, Institut National de Recherche en Informatique et Automatique
France

J.-P. Soucy
Ottawa Hospital—Civic Campus
1053 Carling Avenue
Ottawa (Ontario) K1Y 4E9 Canada

C. Janicki
Hôpital Notre-Dame (CHUM)
1560 rue Sherbrooke Est
Montréal (Québec) H2L 4M1 Canada

Abstract. *Thanks to its ability to yield functionally rather than anatomically-based information, the single photon emission computed tomography (SPECT) imagery technique has become a great help in the diagnostic of cerebrovascular diseases which are the third most common cause of death in the USA and Europe. Nevertheless, SPECT images are very blurred and consequently their interpretation is difficult. In order to improve the spatial resolution of these images and then to facilitate their interpretation by the clinician, we propose to implement and to compare the effectiveness of different existing "blind" or "supervised" deconvolution methods. To this end, we present an accurate distribution mixture parameter estimation procedure which takes into account the diversity of the laws in the distribution mixture of a SPECT image. In our application, parameters of this distribution mixture are efficiently exploited in order to prevent overfitting of the noisy data for the iterative deconvolution techniques without regularization term, or to determine the exact support of the object to be restored when this one is needed. Recent blind deconvolution techniques such as the NAS–RIF algorithm, [D. Kundur and D. Hatzinakos, "Blind image restoration via recursive filtering using deterministic constraints," in Proc. International Conf. On Acoustics, Speech, and Signal Processing, Vol. 4, pp. 547–549 (1996).] combined with this estimation procedure, can be efficiently applied in SPECT imagery and yield promising results.*
 [DOI: 10.1117/1.1426082]

Paper 99056 received Oct. 12, 1999; revised manuscript received May 3, 2001; accepted for publication Sept. 5, 2001.
1017-9909/2002/$15.00 © 2002 SPIE and IS&T.

1 Introduction

Single photon emission computed tomography (SPECT) images are obtained by the measure of radiations (gamma rays) coming from radioactive isotopes injected in the human body. Contrary to other medical imaging techniques, such as x-ray, computer tomography, magnetic resonance imaging, etc., this imagery process is able to give functionally rather than anatomically-based information, such as the metabolic behavior of organs (like the human brain), by measuring and visualizing the level of blood flow. This study of regional cerebral blood flow can aid in the diagnostic of cerebrovascular diseases and brain disorders (e.g., Alzheimer's disease, Parkinson's disease, etc.) by indicating lower, or abnormal higher, metabolic activity in some brain regions.

Due to the peculiar imaging process, SPECT suffers from poor statistics and poor spatial resolution. Poor statistics result from the small number of photons that can be acquired for each image; principally owing to the low sensitivity of the collimator and the low dose of the injected radiopharmaceutical. Factors influencing the spatial resolution are mainly the scattering of the emitted photons and, to a lesser degree, the intrinsic resolution of the camera. Consequently, resulting cross-sectional SPECT images are very blurred and their interpretation by the nuclear physician is often difficult, labor-intensive, and subjective. If the object to be visualized is small compared to the source-to-collimator distance, this degradation phenomenon may be

considered to be approximately shift-invariant and, neglecting noise, this one can be modeled by a convolution process between the true undistorted image and the transfer function of the imaging system.[1] A body of theoretical and experimental work has led to approximate this transfer function [also called the point spread function (PSF)] by a two-dimensional symmetric Gaussian Function.[2,3] In order to improve the spatial resolution of SPECT images, some authors have thus investigated the SPECT image deblurring problem with this class of Gaussian transfer function and by using classical Wiener filter techniques[1,2] or supervised maximum entropy filter-based deconvolution technique.[4] This restoration procedure, also called a deconvolution procedure, is an important consideration in SPECT medical imaging where there may be localized singularities or cold/hot spots in the true image, associated with lesions or tumors. These localized singularities may not be visible in the blurred image, owing to the diffusive effects associated with the convolution process, which averages out differences in neighboring values. A deconvolution scheme could then be very useful in order to detect such singularities by improving the spatial resolution of SPECT images.

Under the assumption that the blur operation is exactly known, many iterative methods have been proposed by the image processing community for tackling this deconvolution procedure and for facing the usual difficulties related to this ill-posed problem. Amongst the existing methods, some of them are structured in the context of regularization problem to make the inversion well behaved.[5–8] Others are unregularized and require a termination criteria in order to stop the iterative procedure at the point where there is a balance between the fit to the image data and the amplification of the noise, inherent to this ill-posed inverse problem.[9–13] Nevertheless, let us note that these supervised deconvolution methods remain limited and sensitive to the assumption made on the nature of the blurring function. Theoretically, the PSF can be measured directly from the SPECT camera by visualizing the blurred result of a point source against a uniform background, but such experiment is generally difficult to obtain in practice and does not necessarily yield a reliable PSF. In applications such as medical imaging, when little is known about the PSF, it can turn out often more relevant to estimate directly the PSF from the observed input image. This problem of simultaneously estimating the PSF (or its inverse) and restoring an unknown image is called ''blind deconvolution'' or ''deconvolution with blur identification.'' Recent techniques exist and can be used in the SPECT imagery context.

In this paper, we propose a comparative study of existing blind or supervised deconvolution methods. We discuss and compare their respective effectiveness for improving the spatial resolution of real brain SPECT images. First, we briefly review classical supervised deconvolution methods which assume the blur is exactly known *a priori* and, in this context, we exploit the two-dimensional Gaussian assumption for the PSF proposed by some authors.[1–3] For the class of the supervised deconvolution technique without regularization term, we present an accurate distribution mixture parameter estimation which takes into account the diversity of the laws in the distribution mixture of a SPECT image. In our application, parameters of this distribution mixture are efficiently exploited in order to find a reliable stopping rule for these iterative methods and then to prevent the amplification of the noise. Then, recent blind deconvolution techniques are briefly presented and tested. We will show that the joint estimation of the image and PSF can lead, for some of them, to better restoration results and also that the Gaussian assumption, proposed by some authors, is only a rough approximation. Finally, for the class of the blind deconvolution technique in which the exact support of the object to be recovered is needed, we propose a novel support-finding algorithm exploiting also the parameters of the aforementioned distribution mixture estimation procedure.

This paper is organized as follows. Section II briefly describes supervised deconvolution methods and recent blind deconvolution techniques that we will compare. In Sec. 3, we detail the distribution mixture parameter estimation procedure. Deconvolution experimental results on phantoms, synthetic and real brain SPECT images are given in Sec. 4. Finally, a conclusion and perspectives are given in Sec. 5.

2 Deconvolution

2.1 *Introduction*

In our application, the degradation of a SPECT image can be represented as the result of a convolution of the true image with a blurring function (the PSF) plus an additive term to model the noise from the physical system. If the imaging system is assumed to be linear and shift invariant, the degradation process can then be expressed by the following linear model:

$$g(x,y) = f(x,y) * h(x,y) + n(x,y),$$

where $g(x,y)$ is the degraded or blurred image, $f(x,y)$ is the undistorted true image, $h(x,y)$ is the PSF of the imaging system and $n(x,y)$ is the additive corrupting noise. In this notation, the coordinates (x,y) represent the discrete pixel locations and $*$ is the discrete linear convolution operator.

2.2 *Supervised Deconvolution Methods*

Assuming that the blurring function $h(x,y)$ is known, the problem is then to determine $f(x,y)$ given the observation $g(x,y)$. This one is generally ill-posed owing to the existence of the additive noise. This means that there is no unique least square solution of minimal norm $\|g(x,y) - f(x,y) * h(x,y)\|^2$. Besides, a small perturbation of the given data produces large deviations in the resulting solution. An appropriate solution may be chosen through proper initialization of the algorithm or by using deterministic prior information about the original image (via a regularization term) to make the inversion well behaved. In this way, iterative approaches have been proposed. Their main advantages are that there is no need to explicitly implement the inverse of an operator and the process may be monitored as it progresses. Some of them are briefly presented in this section and are optimal; in the least square sense, under constraints[5] or not,[9] in the maximum likelihood (ML) sense[10] or in the maximum a posteriori (MAP) sense.[6,11]

2.2.1 *Van Cittert's algorithm*

Van Cittert[12] proposed the following iterative algorithm:

$$\hat{f}_{k+1}(x,y)=\hat{f}_k(x,y)+\alpha[g(x,y)-h(x,y)*\hat{f}_k(x,y)],$$

where α is a convergence parameter generally set to 1. In this iterative scheme, the estimated image $\hat{f}(x,y)$ is modified at each iteration by adding a term proportional to the residual $r(x,y)=g(x,y)-h(x,y)*\hat{f}_k(x,y)$.

2.2.2 *Landweber's algorithm*

Another iterative algorithm, proposed by Landweber *et al.*,[9] is provided by the minimization of the norm $\|g(x,y)-h(x,y)*\hat{f}_k(x,y)\|^2$ and leads to the following iteration,

$$\hat{f}_{k+1}(x,y)=\hat{f}_k(x,y)+\alpha\, h(-x,-y)*[g(x,y) - h(x,y)*\hat{f}_k(x,y)].$$

This algorithm, also called the one step gradient, leads to simply move the estimate $\hat{f}(x,y)$ iteratively in the negative gradient direction.

2.2.3 *Richardson–Lucy's algorithm*

The Richardson–Lucy's (RL) algorithm[10] is an iterative technique which attempts to maximize the likelihood of the restored image by using the expectation maximization algorithm[14] when the image is assumed to come from a Poisson process. This iterative algorithm may be succinctly expressed as

$$\hat{f}_{k+1}(x,y)=\hat{f}_k(x,y)\left[h(-x,-y)*\frac{g(x,y)}{h(x,y)*\hat{f}_k(x,y)}\right].$$

In this form of notation, the division and the multiplication is done point-by-point.

2.2.4 *Tichonov–Miller's algorithm*

This algorithm, also called the constrained least squares restoration, consists in choosing the estimate $\hat{f}(x,y)$ that minimizes the following cost function:

$$\hat{f}(x,y)=\arg\min_f\ [\|g(x,y)-h(x,y)*\hat{f}(x,y)\|^2 + \alpha\|c(x,y)*\hat{f}(x,y)\|^2],$$

where the term $c(x,y)*\hat{f}(x,y)$ generally represents a high pass filtered version of the image $\hat{f}(x,y)$. This is essentially a smoothness constraint which suggests that most images are relatively flat with limited high-frequency activity, and thus it is appropriate to minimize the amount of high-pass energy in the restored image. One typical choice for $c(x,y)$ is the two-dimensional (2D) Laplacian operator. The minimization of the earlier equation leads, with the method of successive approximation, proposed in Ref. 5, to the following iterative estimation scheme for $\hat{f}(x,y)$:

$$\hat{f}_{k+1}(x,y)=\hat{f}_k(x,y)+\beta\{g(x,y)*h(-x,-y) - [A_h(x,y)+\alpha A_c(x,y)]*\hat{f}_k(x,y)\},$$

with $\hat{f}_0(x,y)=\beta\,[g(x,y)*h(-x,-y)]$.

$A_h(x,y)=h(x,y)*h(-x,-y)$ and $A_c(x,y)$ are the autocorrelation functions of $h(x,y)$ and $c(x,y)$, respectively. α is called the regularization parameter which must be carefully chosen for reliable restoration. This iteration converges if $0<\beta<(2/|\lambda_{\max}|)$, where $\lambda_{\max}$ is the largest eigenvalue of the matrix $A_h(x,y)+\alpha A_c(x,y)$.

2.2.5 *Super resolution algorithm*

Assuming Poisson photon distribution in the image, then a Bayesian and MAP derivation has been proposed by Hunt *et al.*[11] This one leads to the following iterative scheme:

$$\hat{f}_{k+1}(x,y)=\hat{f}_k(x,y) \times\exp\left\{\left[\frac{g(x,y)}{h(x,y)*\hat{f}_k(x,y)}-1.0\right]*h(x,y)\right\}.$$

2.2.6 *Molina's algorithm*

Following the Bayesian paradigm, Molina *et al.* have proposed to incorporate prior information to the RL (maximum likelihood) restoration method.[6] In order to model the *a priori* smoothness of the image to be recovered, this one is defined by the following conditional autoregressive model:

$$P_F(\mathbf{f})\propto\exp[-\tfrac{1}{2}\alpha\,\mathbf{f}^t(I-\phi N)\mathbf{f}].$$

In this matrix-vector notation, $\mathbf{f}$ is the true image ordered lexicographically by stacking the rows into a vector. α is the unknown regularization parameter, matrix N is such that $N_{ij}=1$ if cells i and j are spatial four-neighbors (pixels at distance one) and zero otherwise, and scalar ϕ is just less than 0.25. The term $\mathbf{f}^t(I-\phi N)\mathbf{f}$ represents, in matrix notation, the sum of squares of the values $\mathbf{f}_i$ minus ϕ times the sum of $\mathbf{f}_i\mathbf{f}_j$ for neighboring pixels i and j. Following the RL method, which corresponds to MAP estimation with a uniform image prior, Molina *et al.* obtain the following iterative scheme:

$$\hat{f}_{k+1}(x,y)=\mu_k(x,y)\overline{f}_k(x,y)+[1-\mu_k(x,y)]\hat{f}_k(x,y) \times\left[h(-x,-y)*\frac{g(x,y)}{h(x,y)*\hat{f}_k(x,y)}\right].$$

$\mu_k(x,y)=0$ corresponds to the classical RL restoration method (we recall that, in this form of notation, the division and the multiplication are done point-by-point). $\overline{f}_k(x,y)$ is a filtered version of $f_k(x,y)$ in which each pixel is the average of its four-neighbors pixels.

2.3 *Blind Deconvolution Methods*

When little is known about the PSF, a solution for the deblurring problem consists in achieving a blind deconvolu-

tion technique. Blind image deconvolution is the simultaneous estimation of the true image and the PSF from the blurred observation. A commonly used method for blind deconvolution is by minimization of an error metric that optimizes the form of the restored image and the PSF (or its inverse) to fit the various constraints on the form of the solution; typically positivity and known support of the object to be recovered. Steepest descent or conjugate gradient method are generally used to achieve optimization.[15,8] A second method, usually called ''grouped coordinate descent,'' restores the image and the PSF separately in an iterative form. During each cycle either the image or the PSF is held static while the other is updated, generally using one of the standard deconvolution technique.[7,13] In these methods, that alternate between restoration of the image and PSF, iterations do not necessarily have to use the same restoration algorithm. In this section, we describe briefly four recent blind deconvolution techniques stemming from these two different approaches.

2.3.1 *The iterative blind deconvolution method*

The iterative blind deconvolution (IBD) method, proposed by Ayers and Dainty,[7] requires that the image and the PSF be non-negative with known finite support (the support is defined as the smallest rectangle containing the entire object). After an initial guess is made for the true image, the algorithm alternates between the image and Fourier domains, enforcing known constraints in each. The constraints are based upon information available about the image and the PSF. The image domain constraints can be imposed by replacing negative valued pixels within the region of support with zero and nonzero pixels outside the region of support with the background pixel value. The Fourier domain constraint involves a Wiener-like filter for the image and the PSF. This filter allows to efficiently suppress noise amplification resulting from the ill-posed nature of the restoration problem

$$\hat{H}_k(u,v)=\frac{G(u,v)\,\hat{F}^*_{k-1}(u,v)}{|\hat{F}_{k-1}(u,v)|^2+\alpha/|\hat{H}_{k-1}(u,v)|^2},$$

$$\hat{F}_k(u,v)=\frac{G(u,v)\,\hat{H}^*_{k-1}(u,v)}{|\hat{H}_{k-1}(u,v)|^2+\alpha/|\hat{F}_{k-1}(u,v)|^2}.$$

where $H_k(u,v)$, $G(u,v)$, and $F(u,v)$ represent the 2D fast Fourier transform of the PSF, the original image and the true image, respectively. Subscripts denote the iteration number of the algorithm and $(.)^*$ is the complex conjugate of $(.)$. The real constant α represents the energy of the additive noise and must be carefully chosen for reliable restoration. Figure 1 gives an overview of this scheme. The algorithm is run for a specified number of iteration, or until the estimates begin to converge. The major drawback of this method is its lack of reliability; the uniqueness and convergence properties are uncertain and the algorithm is sensitive to the initial image estimate and can exhibit instability.

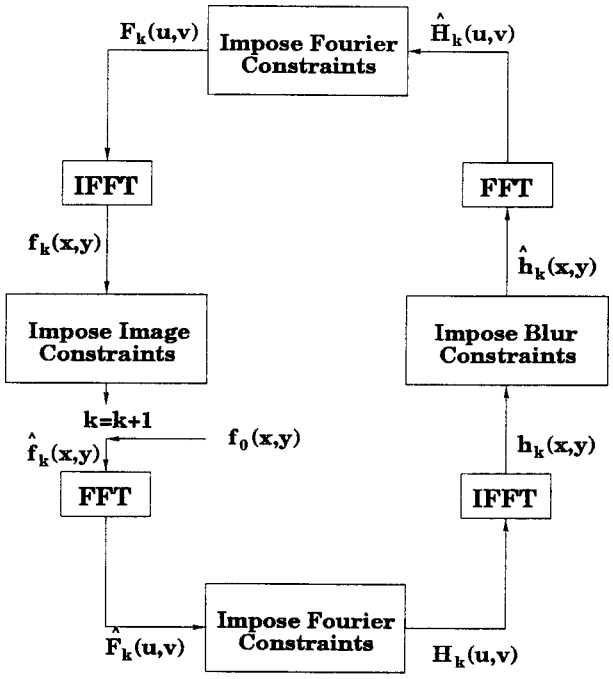

Fig. 1 IBD algorithm.

2.3.2 *The Biggs–Lucy's algorithm*

This method[13] alternates between restoring the image and the PSF using the RL algorithm [by simply swapping variables $h(x,y)$ and $f(x,y)$ in the RL iteration]. The image and the PSF estimates are given by

$$\hat{h}_{k+1}(x,y)=\frac{1}{\sum \hat{f}_k(x,y)}\,\hat{h}_k(x,y)\times\left[f_k(-x,-y)*\frac{g(x,y)}{h_k(x,y)*\hat{f}_k(x,y)}\right],$$

$$\hat{f}_{k+1}(x,y)=\frac{1}{\sum \hat{h}_{k+1}(x,y)}\,\hat{f}_k(x,y)\times\left[h_{k+1}(-x,-y)*\frac{g(x,y)}{h_{k+1}(x,y)*\hat{f}_k(x,y)}\right].$$

This method requires a good initial guess for the PSF and a different number of iterations for the image and the PSF, expressed by an asymmetric factor which is necessary because image and PSF estimates converge at different rates. Depending on the type of the image and the nature of the PSF, this factor is generally different and must be carefully chosen for reliable restoration.

2.3.3 *The non-negativity and support constraints recursive inverse filtering algorithm*

The non-negativity and support constraints recursive inverse filtering (NAS–RIF) technique[15] is applicable to situations in which an object of finite support is imaged against

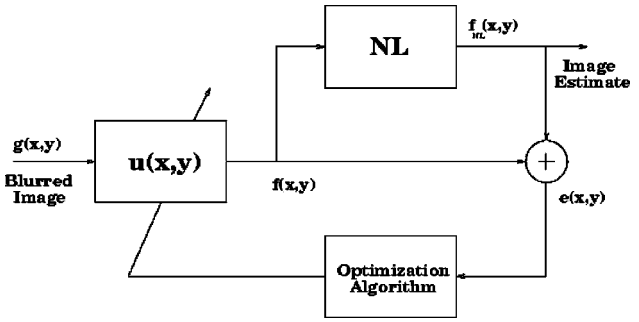

Fig. 2 NAS–RIF algorithm.

a uniform or noisy background which is our case. It comprises a 2D variable finite impulse response filter $u(x,y)$ of dimension $N_{xu}\times N_{yu}$ with the blurred image pixels $g(x,y)$ as input. The output of this filter represents an estimate of the true image $\hat{f}(x,y)$. This estimate is passed through a nonlinear filter which uses a nonexpansive mapping to project the estimated image into the space representing the known characteristics of the true image. The difference between this projected image $\hat{f}_{\mathrm{NL}}(x,y)$ and $\hat{f}(x,y)$ is used as the error signal to update the variable filter $u(x,y)$. Figure 2 gives an overview of this scheme. The image is assumed to be non-negative with known support. The cost function used in this restoration procedure is defined as

$$J(\mathbf{u})=\sum_{(x,y)\in\mathcal{D}_{\mathrm{sup}}}\hat{f}^2(x,y)\left\{\frac{1-\mathrm{sgn}(\hat{f}(x,y))}{2}\right\}+\sum_{(x,y)\in\overline{\mathcal{D}}_{\mathrm{sup}}}[\hat{f}(x,y)-L_B]^2+\gamma\left[\sum_{\forall(x,y)}u(x,y)-1\right]^2,$$

where $\hat{f}(x,y)=g(x,y)*u(x,y)$, and $\mathrm{sgn}(f)=-1$ if $f<0$ and $\mathrm{sgn}(f)=1$ if $f\geqslant 0$. $\mathcal{D}_{\mathrm{sup}}$ is the set of all pixels inside the region of support, and $\overline{\mathcal{D}}_{\mathrm{sup}}$ is the set of all pixels outside the region of support. The variable γ in the third term is nonzero only when L_B is zero, i.e., the background color is black. The third term is used to constrain the parameter away from the trivial all-zero global minimum for this situation. Authors have shown that the earlier equation is convex with respect to $u(x,y)$, so that convergence of the algorithm to the global minimum is ensured using the conjugate gradient minimization routine.[15]

2.3.4 *The You–Kaveh's algorithm*

This method[8] attempts to minimize a cost function consisting of a restoration error measure and two regularization terms, one for the image and the other for the blur

$$C(\hat{f},\hat{h})=\arg\min_{f,h}\left[\tfrac{1}{2}\|g(x,y)-h(x,y)*\hat{f}(x,y)\|^2+\tfrac{1}{2}\lambda\|c(x,y)*\hat{f}(x,y)\|^2+\tfrac{1}{2}\gamma\|a(x,y)*\hat{h}(x,y)\|^2\right],$$

where $a(x,y)$ and $c(x,y)$ are regularization operator (e.g., a high-pass filter such as the Laplacian). λ and γ are the regularization parameters that control the tradeoff between fidelity to the observation and smoothness of the estimated image and the estimated PSF. In order to take into account the scale problem, inherent to this cost function, an alternating minimization using steepest descent or conjugate gradient method is proposed. Note that, using steepest descent method, resulting iterative procedures are close to the iteration scheme proposed by Landweber (with a regularization term for the blur) for the alternate restoration of the image and the PSF.

3 Distribution Mixture Parameter Estimation

3.1 *Introduction*

In this section, we present an estimation procedure allowing to estimate the gray level statistical distribution associated to each class (also called the noise model) of a SPECT image. We will show also how this information can be exploited in the aforementioned supervised or blind deconvolution methods.

To this end, we consider a couple of random fields $Z=(X,G)$, where $G=(G_s,s\in S)$ represents the field of observations located on a lattice S of N sites s (associated to the N pixels of the SPECT image), and $X=(X_s,s\in S)$ the label field (related to the N class labels X_s of a segmented SPECT image). Each aforementioned label is associated to a specific brain anatomical tissue; the ''CSF'' area designates the region that is normally due to the lack of radiations. In this distribution mixture parameter estimation, this region designates the brain region filled with cerebrospinal fluid (without blood flow and thus without radiation) and also the area outside the brain region. The ''white matter'' and ''gray matter'' (brightest region) are associated to a low and a higher level of blood flow, respectively.[16] Each G_s takes its value in $(0,\ldots,255)$ (256 gray levels), and each X_s in ($e_1=$''CSF'', $e_2=$''white matter'', $e_3=$''gray matter'').

In the following, the parameters in upper case letter designate the random variables whereas the lower case letters represent the realizations of these concerned random variables. In this estimation step, the distribution of (X,G) is defined, first, by prior distribution $P_X(x)$, supposed to be Markovian and secondly, by the site-wise conditional likelihoods $P_{G_s/X_s}(g_s/x_s)$ whose shape and parameter $\Phi_{(x_s)}$ depends on the concerned class label x_s (g_s designates the gray level intensity associated to site s). Finally, we assume independence between each random variable G_s given X_s. The observable G is called the ''incomplete data,'' and Z the ''complete data.''

3.2 *Estimation of the Distribution Mixture Parameters for the Complete Data*

Assuming the segmentation result x is known, the parameters of the gray level statistical distribution associated to each class, can then be easily computed with the ML estimator of the complete data.

Experimentations have shown that we can rightly model the statistical gray level distribution in the background or in the CSF area by a exponential law (see Ref. 3 and also the left part of the histogram reported in Fig. 3). This led us to think that the noise in this region is approximately Poissonian with the following statistical gray level distribution:

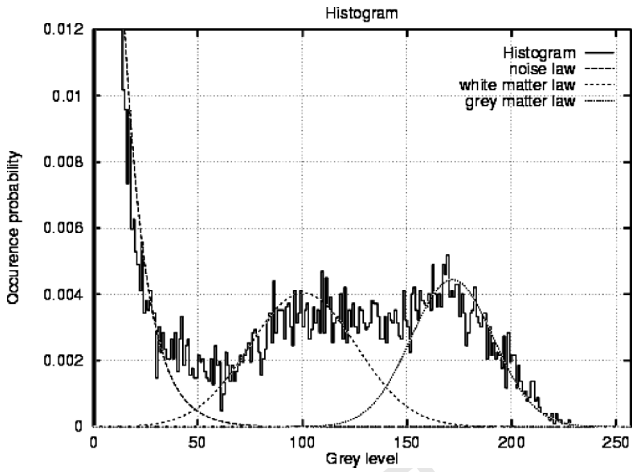

Fig. 3 Image histogram of the picture reported in Fig. 4(b) (solid curve) and estimated probability density mixture obtained with the ICE procedure (dotted and dashed curves).

$$\mathcal{E}_G(g;\alpha)=\frac{1}{\alpha}\exp\left(-\frac{g}{\alpha}\right),$$

with $g>0$. Let now $G=(G_1, ..., G_M)$ be M random variables, independent and identically distributed according to a ''single'' exponential law $\mathcal{E}_G(g;\alpha)$, and $g=(g_1, ..., g_M)$ a realization of G. The ML estimator of α_{ML} for the complete data is simply the mean of the sample g.[17]

In order to describe the luminance within the white matter and the gray matter regions, we model the conditional density function for these regions by two Gaussian laws. This assumption of normality is a reasonable approximation due to the reconstruction physical process used in SPECT imagery in which the gray level of a given pixel, herein considered as a random variable, are sums of many variables and the ''central limit theorem'' can be applied.[17] The corresponding ML estimator of the complete data, for a sample g distributed according to a normal law, is defined simply by the empirical mean and the empirical variance.

3.3 *Estimation of the Distribution Mixture Parameters for the Incomplete Data*

When the segmentation result is unknown (i.e., the class label of each pixel is not supposed to be known), the considered problem is more complex. In order to determine $\Phi=[\Phi_{(e_1)},\Phi_{(e_2)},\Phi_{(e_3)}]$, we use the iterative conditional estimation (ICE) algorithm. This procedure, described in detail in Ref. 18 relies on an estimator $\hat{\Phi}(X,G)$ with good asymptotic properties, like the ML estimator, for completely observed data case. When X is unobservable, this procedure starts from an initial parameter vector $\Phi^{(0)}$ (not too far from the optimal one) and generates a sequence of parameter vectors leading to the optimal parameters, in the least square sense, with the following iterative scheme:

$$\Phi^{(p+1)}=\frac{1}{n}\ \{\hat{\Phi}[x_{(1)},g]+\cdots+\hat{\Phi}[x_{(n)},g]\},$$

where $x_{(i)}$, with $i=1,2,\ldots,n$, , are realizations of X drawn according to the posterior distribution $P_{X/G}[x/g,\Phi^{(p)}]$. In order to decrease the computational load, we can take $n=1$ without altering the quality of the estimation.[19] Finally, we can use the Gibbs sampler algorithm[20] to simulate realizations of X according to the posterior distribution. For the local *a priori* model of the Gibbs sampler, we adopt an isotropic Potts model with a first order neighborhood.[21] In this model, there are two parameters, called ''the clique parameters'' denoted β_1,β_2 and associated to the horizontal and vertical binary cliques, respectively. (Cliques are subsets of sites which are mutual neighbors.[21]) Given this *a priori* model, the prior distribution $P_X(x)$ can be written as

$$P_X(x)=\exp\left\{-\sum_{\langle s,t\rangle}\beta_{st}[1-\delta(x_s,x_t)]\right\},$$

where summation is taken over all pairs of neighboring sites and $\delta(.)$ is the Kronecker delta function. In order to favor homogeneous regions with no privileged orientation in the Gibbs sampler simulation process, we choose $\beta_{st}=\beta_1=\beta_2=1$. Finally, $\Phi^{(p+1)}$ is computed from $\Phi^{(p)}$ in the following way:

- **Stochastic step**: using the Gibbs sampler, one realization x is simulated according to the posterior distribution $P_{X/G}(x/g)$, with parameter vector $\Phi^{(p)}$.
- **Estimation step**: the parameter vector $\Phi^{(p+1)}$ is estimated with the ML estimator of the complete data corresponding to each class.
  - If $N_1=\#(s\in S:x_s=e_1)$ is the number of pixels of the CSF area, the ML estimator $\hat{\Phi}_{(e_1)}$ of α is given by Ref. 17: $\hat{\alpha}(x,g)=(1/N_1)\Sigma_{s\in S:x_s=e_1}g_s$.
  - If $N_2=\#(s\in S:x_s=e_2)$ and $N_3=\#(s\in S:x_s=e_3)$ pixels are located in the white matter and gray matter regions, respectively, the corresponding ML estimator of each class is given by the empirical mean and the empirical variance. For instance, for the white matter class, we have for $\hat{\Phi}_{(e_2)}$:

$$\hat{\mu}(x,g)=\frac{1}{N_2}\sum_{s\in S:x_s=e_2}g_s,$$

$$\hat{\sigma}^2(x,g)=\frac{1}{(N_2-1)}\sum_{s\in S:x_s=e_2}(g_s-\hat{\mu})^2.$$

- Repeat until convergence is achieved; i.e., if $\hat{\Phi}^{(p+1)}\neq\hat{\Phi}^{(p)}$, we return to stochastic step.

Figure 3 represents the estimated distribution mixture of the SPECT image shown in Fig. 4(b). The three site-wise likelihoods $P_{G_s/X_s}(g_s/e_k)$, $k=1,2,3$, (weighted by the estimated proportion π_k of each class e_k) are superimposed to the image histogram. Corresponding estimates obtained by the estimation procedure, requiring about ten iterations, are given in Table 1.

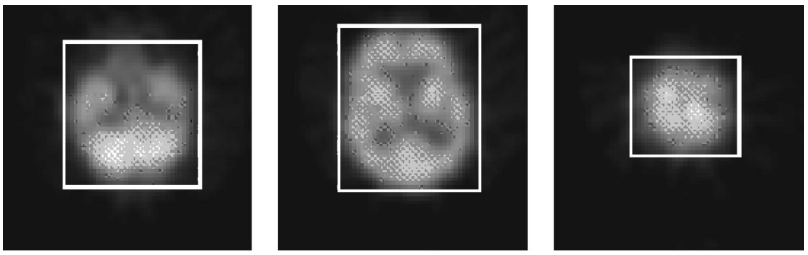

Fig. 4 Examples of support determination for some cross-sectional brain SPECT slices.

3.4 *Determination of the Support and Stopping Rule*

In the case of supervised deconvolution techniques without regularization term, such as the Van–Cittert, the Landweber, the RL, and the super resolution algorithms, the iterative deconvolution procedure is generally monitored as it progresses and stopped after some iterations, generally by visual inspection. This iteration number may be very different for each SPECT image and is generally related to the behavior of each iterative method near the convergence. In fact, at some point of the iteration procedure, the solution fit more to the noise than the image data. Therefore, for these methods, the process has to be stopped at the point where there is a balance between the fit to the image data and the amplification of noise. To this end, in order to stop automatically these algorithms before the amplification of the noise, we propose to compute the parameters of the distribution mixture of $\hat{f}_k$ regularly, namely every k iterations (k depends on the speed of convergence of the considered deconvolution method). If the parameter associated to the background noise (i.e., α) is above a fixed threshold, we decide to stop the procedure. Of course, this threshold has to be fixed empirically like the iteration number. Nevertheless, contrary to the iteration number, this threshold does not depend of the adopted unregularized method or the speed of convergence of each method as well as the used SPECT images. Besides, it does not require a visual inspection, for each iteration of the deconvolution procedure, that can be cumbersome and unreliable for an automatic deconvolution of a set of SPECT images.

For the supervised deconvolution methods using a regularization term (e.g., the Tichonov–Miller's algorithm), or prior information (e.g., the Molina's algorithm), the termination criteria consists simply in stopping the algorithm when the solution is stable. Nevertheless these methods require a regularization parameter which must be chosen carefully for reliable restoration. This parameter can be also derived efficiently from the proposed noise model estimation procedure.

In the case of blind deconvolution techniques, in which the rectangular support of the object to be restored is needed and unknown, we can also efficiently exploit the parameters of the distribution mixture of the input image g by adopting the following strategy; we assume that the row $\mathcal{R}_i \in S$ contains the object $\mathcal{O}$ to be restored if we can find two consecutive sites $\in \mathcal{R}_i$ for which

$$P(g_{ij}/\text{"CSF"}) \leqslant P(g_{ij}/\text{"white matter"}),$$

where the subscripts i,j refer to the pixel located at the ith row and the jth column and g to the luminance. We adopt an identical reasoning for the column and the object support is then accurately determined by the set of pixels g_{ij} which belong to a row $\mathcal{R}_i$ and a column $\mathcal{C}_j$ containing the object $\mathcal{O}$. Figure 4 displays examples of rectangular support determination for some cross-sectional brain SPECT images. A more accurate support could be given by an unsupervised Markovian segmentation based on parameters given by the ICE procedure. Finally, let us recall also that for these blind deconvolution techniques, there is no need to implement a stopping rule and convergence is reached when the estimated PSF and image are stable.

Table 1 Estimated parameters for the picture reported in Fig. 4(b). π stands for the proportion of the three classes within the SPECT image. α are the exponential law parameter. μ and σ^2 are the Gaussian law parameters.

	ICE procedure
$\Phi^{\text{final}}_{(e_1)}$	$0.52_{(\pi)}\,11_{(\alpha)}$
$\Phi^{\text{final}}_{(e_2)}$	$0.26_{(\pi)}\;\;100_{(\mu)}\;\;648_{(\sigma^2)}$
$\Phi^{\text{final}}_{(e_3)}$	$0.22_{(\pi)}\;\;172_{(\mu)}\;\;383_{(\sigma^2)}$

4 Experimental Results

The effectiveness of each deconvolution method was tested on several cross-sectional phantoms, synthetic and real hu-

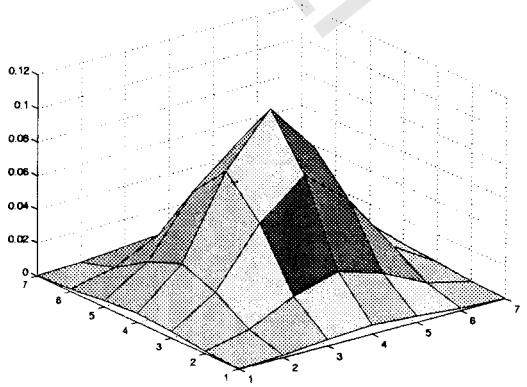

Fig. 5 Original PSF defined as a two-dimensional Gaussian distribution with variance $\sigma^2 = 1.5$ in a 7×7 support.

Table 2 Iteration number for each supervised deconvolution method as chosen by the proposed stopping rule. Respectively, the Van Cittert (VC), the Landweber (LW), the Richardson–Lucy (RL), the super resolution (SR), and the Molina's (MO) algorithms.

Iteration number					
VC	LW	RL	TM	SR	MO
10	4	200	50	100	10

Table 3 Computational cost for each deconvolution method. Respectively, the Van Cittert (VC), the Landweber (LW), the Richardson–Lucy (RL), the super resolution (SR), the Molina (MO), the IBD, the Biggs–Lucy (BL), the NAS–RIF and finally, the You–Kaveh's (YK) algorithm. Results are obtained on a standard Sun-Sparc 2 workstation and are expressed in seconds.

Computational cost									
Supervised methods						Blind methods			
VC	LW	RL	TM	SR	MO	IBD	BL	NAS–RIF	YK
3	1	18	8	18	2	30	120	129	345

man brain SPECT images of 64 × 64 pixels size with 256 gray levels. Those presented in this section are only a few examples.

Except for the Tichonov–Miller's algorithm, the initial estimated image of these iterative schemes is the original input image [i.e., $\hat{f}_0(x,y)=g(x,y)$]. Besides, except for the NAS–RIF blind deconvolution technique, the original PSF estimate, *a priori* fixed for the supervised deconvolution methods, is approximated for the real SPECT images by a two-dimensional Gaussian distribution [i.e., $\hat{h}_0(x,y)=\mathcal{G}_{x,y}(\sigma^2)$] with variance $\sigma^2=1.5$ (i.e., about 3 pixels of width at half maximum as shown in Fig. 5). This variance value has been chosen empirically, for each set of deconvolution experiments presented in this section, in order to obtain the best supervised restoration results. The initial inverse finite impulse response (FIR) filter required by the NAS–RIF algorithm is simply the Kronecker delta function[15] and we have used $\gamma=0$ because the background of the SPECT images is not completely black. Finally, parameters λ and γ, used in the You and Kaveh's algorithm, are given by the estimation method proposed by the authors in Ref. 8. In order to objectively compare the spatial resolution improvements and the contrast enhancement between the original and estimated images as well as the resolution improvement of these different restoration approaches, we have stretched the histogram of the estimated image at convergence [i.e., $\hat{f}_{\text{final}}(x,y)$] in order to get the same mean value as the original input image $g(x,y)$.

For the unregularized supervised deconvolution methods, the termination criteria is given by the stopping strategy presented in Sec. 3.4 (see Table 2). For the blind deconvolution methods requiring the exact support of the object to be restored, deconvolution results are based on the support-finding algorithm presented in this same section.

The computational cost for a SPECT image and for each supervised or blind deconvolution procedure is indicated in Table 3.

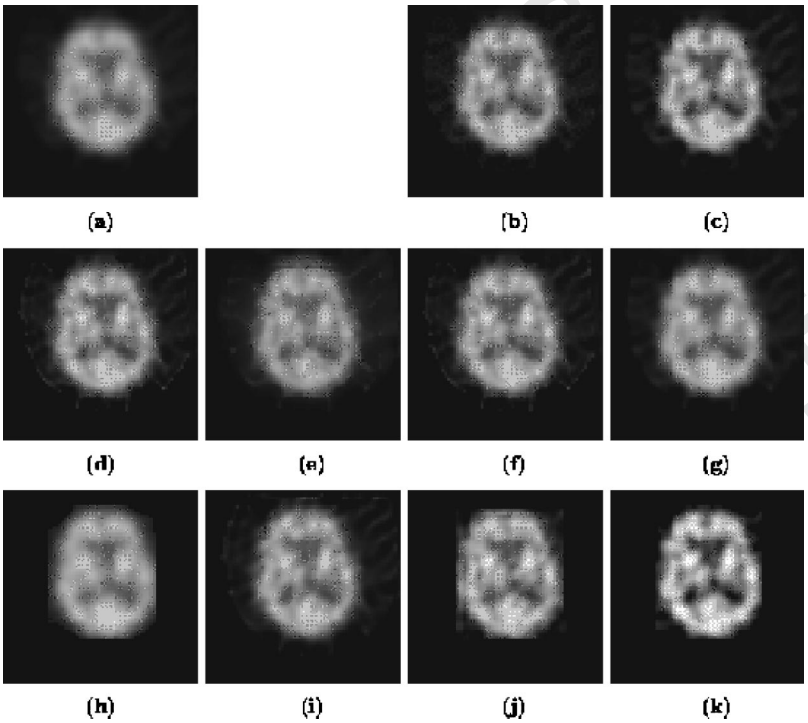

Fig. 6 Examples of brain SPECT image deconvolutions. (a) Original image. (b)–(g) Supervised deconvolution methods, respectively; (b) Van Cittert, (c) Landweber, (d) RL, (e) Tichonov–Miller, (f) super resolution, (g) Molina's algorithm. (h)–(k) Blind deconvolution methods, respectively; (h) IBD, (i) Biggs–Lucy, (j) You–Kaveh, (k) NAS–RIF algorithm.

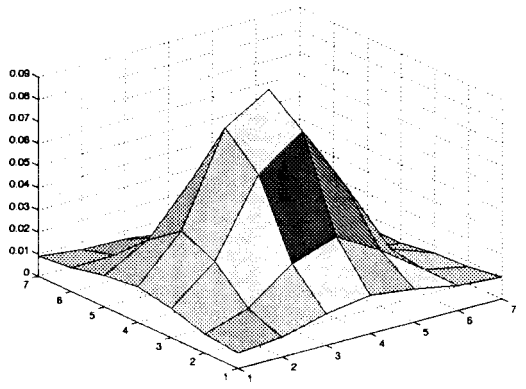

Fig. 7 Estimated PSF by the You–Kaveh's algorithm in a 7×7 support.

Figures 6 presents examples of brain SPECT image deconvolutions obtained by these different methods. Figure 7 displays the PSF estimated by the You–Kaveh's algorithm.

Amongst the supervised deconvolution schemes, the Van Cittert's method seems to improve slightly the resolution of the original SPECT image. The Landweber's algorithm seems to give quite good results relatively to its implementation simplicity and its low computational complexity. The Tichonov–Miller and the Molina's algorithms, which impose *a priori* smoothness of the true image in an effort to control noise, seem to fail to detect all details and singularities of the true undistorted image. In fact, the used prior model seems to be much too simple to model accurately all the property of the true unblurred image. The RL and the super resolution algorithms give similar results and allow to improve slightly the spatial resolution of these SPECT images.

Amongst the blind deconvolution techniques, the IBD is unable to converge for 200 iterations and more. The algorithm fails to produce a reliable estimate of the true image for all the presented SPECT images. Deconvolution experiments with the exact rectangular support of the object to be restored, various initial conditions and different noise parameter values α produced poor results as well. The Biggs–Lucy and the You–Kaveh's algorithms seem to give quite good contrast enhancement results but also show undesirable artifacts all around (and maybe inside) the object to be restored. In addition, these techniques remain sensitive to the initial PSF given to the deconvolution procedure. A random initial guess for the PSF or an initial Kronecker delta function lead to poor results. Let us note that these methods are not ensured to converge to the global *minima* and remain highly sensitive to the initial conditions. Finally, the NAS–RIF technique seems to converge to a good estimate of the solution without *a priori* information or good initial guess about the PSF. Figure 8 gives examples of five cross-sectional SPECT image deconvolutions of human brain given by the NAS–RIF algorithm.

The effectiveness of these deconvolution techniques is also tested on a real SPECT phantom (i.e., a physical plexiglas head phantom filled with radioactive material and measured by a SPECT system) for which the ground truth of this segmented phantom is exactly known and thus for which the performance of each deconvolution method can then be objectively judged. Figure 9 presents an example of deconvolution results, on this SPECT phantom, obtained by the different aforementioned deconvolution methods. We can easily notice that this SPECT volume is less noisy and less blurred than the real human brain SPECT slice previously presented and processed (due to several factors such as a different dose of radioactive isotopes contained in each uniform region of this SPECT phantom, a longer acquisition time, the stillness of this simulated brain during the SPECT process, a reduced attenuation, etc.). In order to fully assess the success of this restoration procedure, we use the specific evaluation criteria proposed in Ref. 4, based on the estimation of the three following measures:

i. First, the average contrast of the image, defined by $C=(1-m_2/m_3)$, where m_2 and m_3 are the mean of the pixel value in the white matter and gray matter area, respectively.

ii. (ii) Second, the image mottle M_2 in the white matter region, characterized by taking the ratio of the standard deviation σ_2 of pixel values in this area to the mean m_2.

iii. (iii) Third, the image mottle M_3 in the gray matter area.

These two last parameters allow to measure the amplification of the noise and/or measure the presence of undesirable artifacts that can be created by the deconvolution procedure in a uniform region of the real SPECT phantom (thus with ideally uniform radioactive activity). Due to the difference of proportion of pixels belonging to each brain

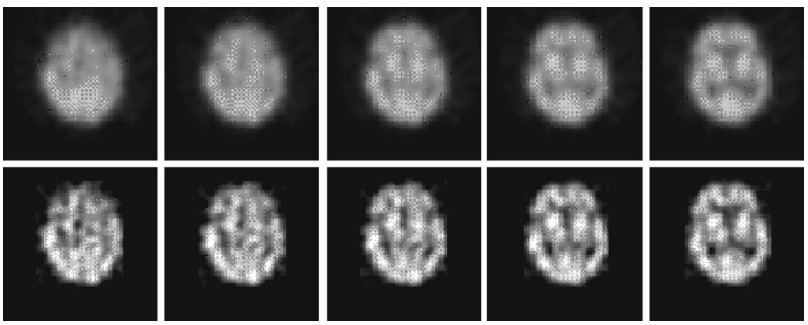

Fig. 8 Examples of human brain cross-sectional SPECT image deconvolutions given by the NAS–RIF algorithm. Top: five consecutive real cross-sectional SPECT slices. Bottom: deconvolution results.

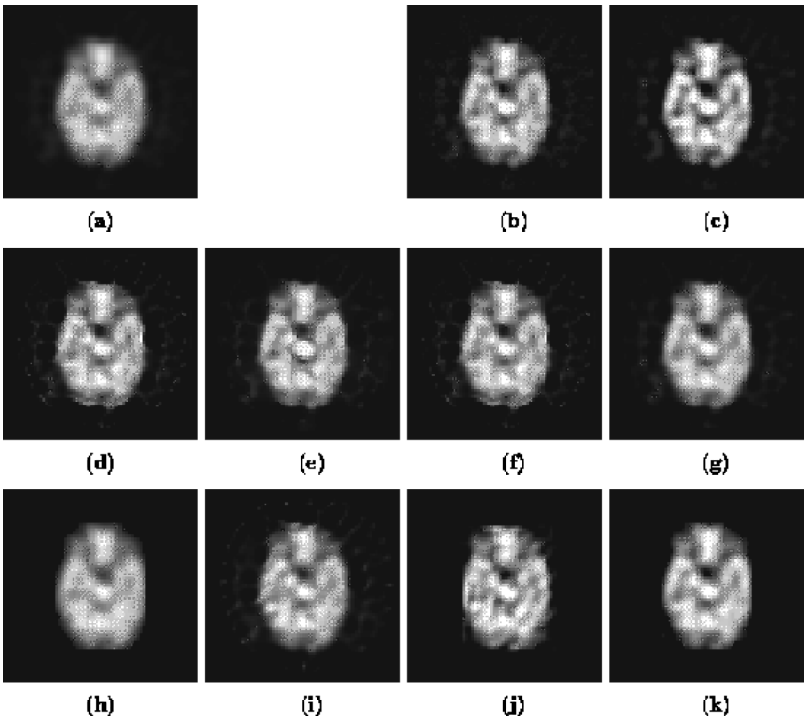

Fig. 9 Examples of phantom SPECT image deconvolutions. (a) Original image. (b)–(g) Supervised deconvolution methods, respectively; (b) Van Cittert, (c) Landweber, (d) RL, (e) Tichonov–Miller, (f) super resolution, (g) Molina's algorithm. (h)–(k) Blind deconvolution methods, respectively; (h) IBD, (i) Biggs–Lucy, (j) You–Kaveh, (k) NAS–RIF algorithm.

anatomical tissue, we consider the total mottle measure given by $M = \rho_2 M_2 + \rho_3 M_3$, with ρ_2 and ρ_3 designates the proportion of pixel belonging to the white matter and gray matter area, respectively. A reliable SPECT image restoration technique will then allow to enhance the contrast of the image with little increase in mottle, i.e., without amplifying too much the noise and/or without creating false artificial features (technically, an increase by a factor of 10%–15% of the original mottle of the image remains acceptable if the contrast enhancement is significantly increased).[4] Due to the difference of thickness between the cross-sectional slices of the real and segmented phantom, these abovementioned measures are estimated on the whole three-dimensional (3D) phantom after this one has been registered[22] on the ground truth of the segmented phantom volume (see Fig. 10 where some consecutive slices of the segmented phantom are shown). Table 4 gives the contrast and image mottle for each deconvolution technique applied on this SPECT phantom.

Amongst the supervised deconvolution schemes, the Landweber's algorithm allows to increase significantly the contrast of the image but at cost of an unacceptable increase of the mottle of the image (+33.0% of mottle). Deconvolution results, obtained on this SPECT phantom, by the Van Cittert, the RL, the Tichonov–Miller and the super resolution algorithm are nearly similar; they allow to obtain a good contrast enhancement but also present some artifacts, visible all around the object to be restored. Molina's algorithm gives the best results for this SPECT volume; i.e., a good contrast enhancement with only a little increase of the mottle. Experiments have shown that this method is well suited for cross-sectional SPECT images not too blurred.

Amongst the blind deconvolution techniques, the IBD algorithm fails to produce a reliable estimate of the true image. The You–Kaveh's algorithm allows one to increase the contrast of the image but this technique also creates undesirable artifacts and/or an unacceptable amplification of the noise (+30.2% of mottle). Deconvolution result given by the Biggs–Lucy's algorithm is very poor. Finally, the NAS–RIF blind deconvolution technique produce contrast enhancement result as good as the best supervised deconvolution technique (i.e., the Molina's algorithm) along with the slightest increase of the mottle amongst the con-

Fig. 10 Examples of some consecutive cross-sectional slices of the segmented phantom (ground truth).

Table 4 Contrast and image mottle enhancement from the original input image and for each deconvolution method (enhancement expressed in percentage). Respectively; the Van Cittert (VC), the Landweber (LW), the Richardson–Lucy (RL), the super resolution (SR), the Molina (MO), the IBD, the Biggs–Lucy (BL), the NAS–RIF and finally, the You–Kaveh's (YK) algorithm.

	Supervised						Blind			
	VC	LW	RL	TM	SR	MO	IBD	BL	NAS–RIF	YK
ΔC	34.5%	62.0%	35.1%	28.7%	35.1%	28.0%	−6.1%	12.2%	24.7%	29.0%
ΔM	15.3%	33.0%	14.9%	13.5%	14.9%	12.6%	3.8%	13.8%	11.5%	30.2%

sidered supervised and blind deconvolution techniques. Experiments have shown that this method is well suited for both very blurred SPECT slices and also in the case of less blurred SPECT images.

We have also tested the effectiveness of these deconvolution techniques on a cross-sectional slice of a synthetic SPECT volume. In order to simulate at best the typical characteristics of real human brain SPECT images, we have recreated three homogeneous regions and added the corresponding noise for each ones, according to the gray level statistical distribution already estimated on a real human brain SPECT slice (see the distribution mixture presented in Fig. 3 and parameters given in Table 1). We have also added a 3D Gaussian blur in order to simulate the 3D scattering of the emitted photons. Figure 11 shows the ground truth of a segmented synthetic slice, the synthetic SPECT slice, and finally the deconvolution results obtained by our different restoration methods.

Amongst the supervised deconvolution schemes, the Van Cittert and the Landweber's algorithm give quite good results although at cost of a slight amplification of the noise in each uniform region of the synthetic SPECT slice. The

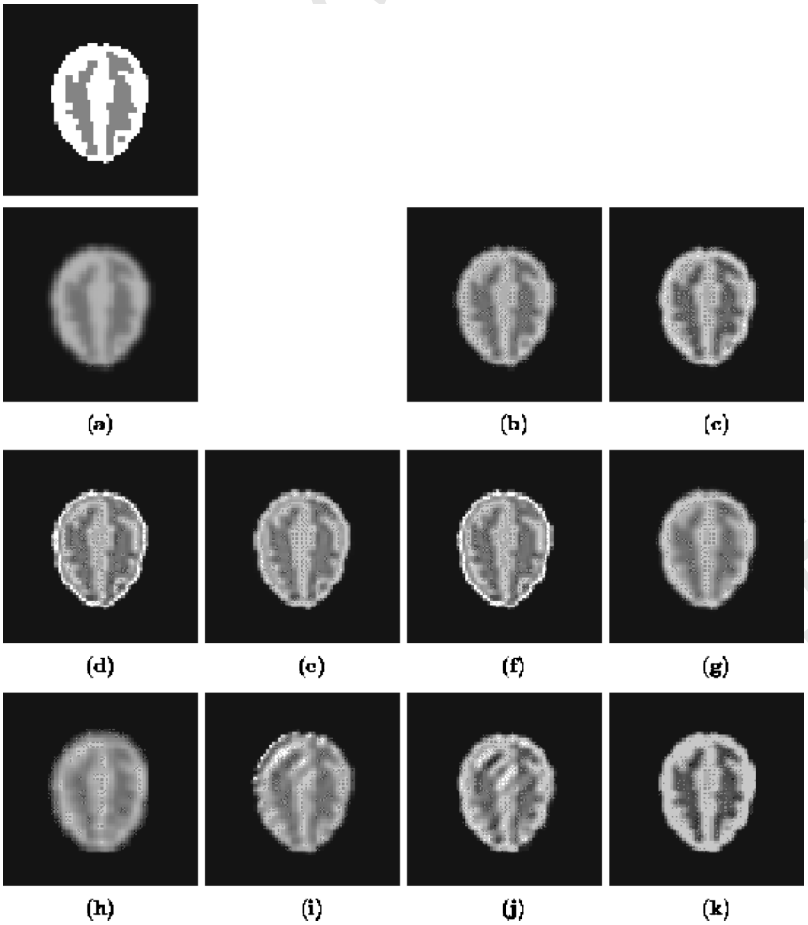

Fig. 11 Examples of synthetic SPECT image deconvolutions. (a) Top: ground truth of the segmented synthetic slice. Bottom: synthetic SPECT slice. (b)–(g) Supervised deconvolution methods, respectively; (b) Van Cittert, (c) Landweber, (d) RL, (e) Tichonov–Miller, (f) super resolution, (g) Molina's algorithm. (h)–(k) Blind deconvolution methods, respectively; (h) IBD, (i) Biggs–Lucy, (j) You–Kaveh, (k) NAS–RIF algorithm.

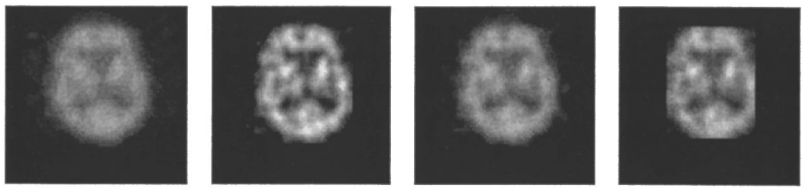

Fig. 12 (a) Cross-sectional slice of a phantom SPECT volume, (b) deconvolution with the optimal parameters given by our distribution mixture estimation method [a rectangle of 35 × 43 pixels size in this case, see Fig. 4(b)], (c) overestimated support size (37 × 45 pixels size), (d) underestimated support size (33 × 41 pixels size).

RL, the Tichonov–Miller and the super resolution algorithm show clearly some artifacts all around the object to be restored. Deconvolution result given by the Molina's algorithm is very poor for this synthetic image; experiments have shown that this method is not well suited for highly blurred image.

Amongst the blind deconvolution techniques, the IBD does not converge. The You–Kaveh and the Biggs–Lucy's algorithm show clearly false and undesirable artificial features created by the iterative blind deconvolution procedure. Once again, the NAS–RIF technique produces a relatively good restoration result.

Finally, in order to attest the effectiveness of our parameter estimation procedure, we have also compared the deconvolution results, on SPECT images, obtained by exploiting or not the optimal parameters given by our distribution mixture estimation method.

Figure 12 shows the results of the NAS–RIF algorithm, on a cross-sectional slice of a phantom SPECT volume, for respectively, the rectangular support estimated by our procedure [a rectangle of 35 × 43 pixels size in this case, see Fig. 4(b)], an overestimated support size (37 × 45 pixels size), and finally an underestimated support size (33 × 41 pixels size). These experiments clearly show that the restoration, even for an overestimation or underestimation of 10%, produces less good deconvolution results compared to the one obtained by exploiting the rectangular support estimated by our estimation procedure. In the case of an overestimated (and incorrect) support size, the blind deconvolution technique does not improve sufficiently the resolution of the SPECT image [cf. Fig. 12(c)]. Moreover, in the case of an underestimated support size, some external regions of the brain are missing [cf. Fig. 12(d)]. The other blind deconvolution algorithms produce poor deconvolution results for underestimation or overestimation of support size as well. This leads us to think that a good estimation of the support size is given by our algorithm and this accurate estimation is essential in order to rightly constrain the ill-posed nature of the blind deconvolution algorithms.

As for unregularized supervised deconvolution methods, Fig. 13 shows the results of $N=4$ iterations of the Landweber's algorithm (as chosen by the proposed stopping rule and by setting $\alpha<\alpha_0$ where α_0 is the parameter associated to the background noise for the original input image) and the deconvolution result given by $N=2$ and $N=6$ iterations of this iterative algorithm. For $N=2$, the deconvolution result is poor (the brain remains blurred) and for $N=6$ the amplification of noise begins to be too important. Therefore, $N=4$ (chosen by our algorithm) seems to be a good compromise solution. In fact, the contrast enhancement increases with the number of iteration until $N=4$ and keeps nearly constant after $N=4$ (at around $\Delta C=+60\%$). For $N=6$ and over, the mottle of the image begins to significantly increase to unacceptable levels.

5 Conclusion

In this paper we have shown that a deconvolution procedure noticeably improves the spatial resolution of human brain SPECT images and can be a great help to facilitate their interpretation by the nuclear physician. The proposed distribution mixture estimation procedure allows efficiently to give a reliable termination criteria for the unregularized iterative deconvolution techniques or to accurately determine the rectangular support of the object to be restored when this one is needed by some blind deconvolution techniques. This estimation procedure is quite general and can be used for other applications such as an unsupervised Markovian segmentation of brain SPECT images into different anatomical tissues, to create realistic synthetic brain

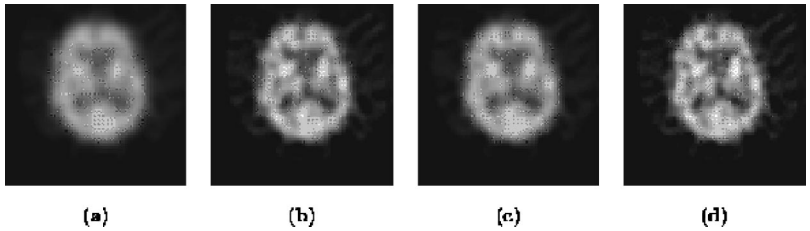

Fig. 13 (a) Cross-sectional slice of a phantom SPECT volume. (b) $N=4$ iterations of the Landweber's algorithm (as chosen by the proposed stopping rule). (c) $N=2$ iterations of the Landweber's algorithm. (d) $N=6$ iterations of the Landweber's algorithm.

SPECT images or to give relevant information in order to classify these brain images into different pathology classes. Amongst existing deconvolution techniques, the NAS–RIF algorithm performs better than other deconvolution schemes for SPECT image restoration. This technique can be efficiently combined with our estimation procedure to find the support of the object to be restored and yield very promising results without *a priori* assumption on the nature of the blurring function or for all type of SPECT images (more or less blurred). Finally, let us note also that this method can efficiently be extended in order to take into account the inter-slice blur inherent to this 3D imaging process. This can be done by considering a 3D variable FIR filter with a blurred SPECT volume pixels as input.[23]

Acknowledgment

The authors thank INRIA (Institut National de la Recherche en Informatique et Automatique, France) for financial support of this work (postdoctoral grant).

References

1. D. Boulfelfel, R. M. Rangayyan, L. J. Han, and R. Kloiber, ''Prereconstruction restoration of myocardial single photon emission computed tomography images,'' *IEEE Trans. Med. Imaging* **11**(3), 336–341 (1992).
2. M. T. Madsen and C. H. Park, ''Enhancement of SPECT images by Fourier filtering the projection set,'' *J. Nucl. Sci. Technol.* **26**, 2687–2690 (1979).
3. T. S. Curry, J. E. Dowdey, and R. C. Murry, *Christensen's Physics of Diagnostic Radiology*, Lea and Febiger (1990).
4. S. Webb, A. P. Long, R. J. Ott, M. O. Leach, and M. A. Flower, ''Constrained deconvolution of SPECT liver tomograms by direct digital image restoration,'' *Med. Phys.* **12**(1), 53–58 (1985).
5. A. K. Katsaggelos, J. Biemond, R. W. Shafer, and R. M. Mersereau, ''A regularized iterative image restoration algorithm,'' *IEEE Trans. Acoust., Speech, Signal Process.* **39**, 914–929 (1991).
6. R. Molina, J. Mateos, and J. Abad, ''Prior models and the Richardson–Lucy restoration method,'' *Restoration HST Images Spectra II* **52**, 118 (1994).
7. G. R. Ayers and J. C. Dainty, ''Iterative blind deconvolution method and its application,'' *Opt. Lett.* **13**(7), 547–549 (1988).
8. Y. L. You and M. Kaveh, ''A regularization approach to joint blur identification and image restoration,'' *IEEE Trans. Image Process.* **5**(3), 416–428 (1996).
9. L. Landweber, *Am. J. Math.* **73**, 615 (1951).
10. L. B. Lucy, ''An iterative technique for the rectification of observed images,'' *Astron. J.* **79**(6), 8–37 (1974).
11. B. R. Hunt and P. J. Sementilli, ''Description of a poisson imagery super-resolution algorithm,'' *Astronomical Data Analysis Software and Systems I* **52**, 196–199 (1992).
12. P. H. Van Cittert, *Z. Phys.* **69**, 298 (1931).
13. D. S. C. Biggs and M. Andrews, ''Asymmetric iterative blind deconvolution of multiframe images,'' *Proc. SPIE* **3461**, 33 (1998).
14. A. P. Dempster, N. M. Laird, and D. B. Rubin, ''Maximum likelihood from incomplete data via the EM algorithm,'' *Royal Statistical Society* ■■, 1–38 (1976).
15. D. Kundur and D. Hatzinakos, ''Blind image restoration via recursive filtering using deterministic constraints,'' in *Proc. International Conf. On Acoustics, Speech, and Signal Processing*, Vol. 4, pp. 547–549 (1996).
16. D. C. Costa and P. J. Ell, *Brain Blood Flow in Neurology and Psychiatry*, P. J. Ell, Ed. (1991).
17. S. Banks, *Signal Processing, Image Processing and Pattern Recognition*, Prentice Hall, Englewood Cliffs, New Jersey (1990).
18. F. Salzenstein and W. Pieczinsky, ''Unsupervised Bayesian segmentation using hidden markovian fields,'' in *Proc. Int. Conf. On Acoustics, Speech, and Signal Processing*, pp. 2411–2414 (May 1995).
19. B. Braathen, P. Masson, and W. Pieczynski, ''Global and local methods of unsupervised Bayesian segmentation of images,'' *Graphics Vision* **2**(1), 39–52 (1993).
20. S. Geman and D. Geman, ''Stochastic relaxation, Gibbs distributions and the Bayesian restoration of images,'' *IEEE Trans. Pattern Anal. Mach. Intell.* **6**(6), 721–741 (1984).
21. J. Besag, ''On the statistical analysis of dirty pictures,'' *J. R. Statistical Soc.* **B-48**, 259–302 (1986).
22. K. J. Friston, J. Ahburner, C. D. Frith, J. B. Poline, J. D. Heather, and R. S. J. Frackowiak, ''Spatial registration and normalization of images,'' *Hum. Brain Mapping* **3**(3), 165–189 (1995).
23. M. Mignotte and J. Meunier, ''Three-dimensional blind deconvolution of SPECT images,'' *IEEE Trans. Biomed. Eng.* **47**(2), 274–281 (2000).

Max Mignotte received his DEA (postgraduate degree) in digital signal, image and speech processing from the INPG University, France (Grenoble), in 1993 and his PhD degree in electronics and computer engineering from the University of Bretagne Occidentale (UBO) and from the digital signal laboratory (GTS) of the French Naval Academy, France, in 1998. He was an INRIA postdoctoral fellow at the University of Montreal (DIRO), Canada (Québec), from 1998 to 1999. He is currently with DIRO at the Computer Vision and Geometric Modeling Lab as an Assistant Professor at the University of Montréal. His current research interests include statistical methods and Bayesian inference for image segmentation (with hierarchical Markovian, statistical templates, or active contour models), parameters estimation, tracking, classification, deconvolution, and restoration issues in medical or sonar imagery.

Jean Meunier received his BSc degree in physics from the University of Montréal in 1981, his MScA degree in applied mathematics in 1983, and his PhD in biomedical engineering in 1989 from Ecole Polytechnique de Montréal. In 1989, after postdoctoral studies at the Montreal Heart Institute, he joined the department of computer science at the University of Montréal, where he is currently a full professor. He is also a regular member of the Biomedical Engineering Institute at the same institution. His research interests are in computer vision and its applications to medical imaging. His current research focuses on motion assessment and analysis in biomedical images.

J.-P. Soucy went to the College Stanislas de Montréal, and received his "baccalauréat français" (with honors) from the Académie de Caën in 1975. He then went on to the Université de Montréal Faculty of Medicine, graduating first in his class in 1980. Nuclear medicine training then followed at the Université de Montréal and McGill University, with certifications from the Physicians' College of the Province of Quebec, from the Royal College of Physicians and Surgeons of Canada, and from the American Board of Nuclear Medicine in 1984. He then spent a year as a fellow of the McLaughlin Foundation in Service Hospitalier Frédéric-Joliot, Orsay, France, doing cerebral blood flow studies in stroke and dementia patients under the supervision of Dr. Claude Raynaud. Dr. Soucy has practiced Nuclear Medicine at the Hôpital Notre-Dame, Montréal, later incorporated into the Université de Montréal Health Sciences Center (CHUM), from 1985 to 2000. He is still on staff at that hospital but since September of 2000 he has practiced at The Ottawa Hospital. He was Chief of the Department of Nuclear Medicine at CHUM from 1997 to 2000, and Chief of Residency training in nuclear medicine at the University of Montreal from 1994 to 2000. He is a professor of medicine, division of nuclear medicine, at the Faculty of Medicine of the Ottawa University, and a professor of radiology (clinical) at the Faculty of Medicine of the University of Montreal.

Christian Janicki received his BSc degree in physics from the University of Montreal in 1981, his MSc degree in physics in 1982, and his PhD in 1988. He joined the Centre Canadien de fusion magnétique (CCFM) in 1988, where he worked on x-ray tomographic imaging of the tokamak plasma, heat transport, and bremsstrahlung emission from relativistic electrons. He joined the biomedical physics group at the Centre Hospitalier de l'Université de Montréal (CHUM) in 1995. His current research interests include 3D SPECT imaging, beta and gamma dosimetry modeling, and intravascular brachytherapy.